https://doi.org/10.1016/j.jmst.2021.06.055
This is the Pre-Published Version.

Cu-assisted austenite reversion and enhanced TRIP effect in maraging stainless steels

M.C. Niu[a,b,c], K. Yang[b], J.H. Luan[d], W. Wang[b,*], Z.B. Jiao[c,e,*]

[a] *School of Materials Science and Engineering, University of Science and Technology of China, Shenyang 110016, China*

[b] *Shi-changxu Innovation Center for Advance Materials, Institute of Metal Research, Chinese Academy of Sciences, Shenyang 110016, China*

[c] *Department of Mechanical Engineering, The Hong Kong Polytechnic University, Hong Kong, China*

[d] *Department of Materials Science and Engineering, City University of Hong Kong, Hong Kong, China*

[e] *The Hong Kong Polytechnic University Shenzhen Research Institute, Shenzhen, Guangdong, China*

* *Corresponding authors: wangw@imr.ac.cn (W. Wang); zb.jiao@polyu.edu.hk (Z.B. Jiao).*

Abstract

Control of the formation and stability of reverted austenite is critical in achieving a favorable combination of strength, ductility, and toughness in high-strength steels. In this work, the effects of Cu precipitation on the austenite reversion and mechanical properties of maraging stainless steels were investigated by atom probe tomography, transmission electron microscopy, and mechanical tests. Our results indicate that Cu accelerates the austenite reversion kinetics in two manners: first, Cu, as an austenite stabilizer, increases the equilibrium austenite fraction and hence enhances the chemical driving force for the austenite formation, and second, Cu-rich nanoprecipitates promote the austenite reversion by serving as heterogeneous nucleation sites

© 2022. This manuscript version is made available under the CC-BY-NC-ND 4.0 license http://creativecommons.org/licenses/by-nc-nd/4.0/

and providing Ni-enriched chemical conditions through interfacial segregation. In addition, the Cu precipitation hardening compensates the strength drop induced by the formation of soft reverted austenite. During tensile deformation, the metastable reverted austenite transforms to martensite, which substantially improves the ductility and toughness through a transformation-induced plasticity (TRIP) effect. The Cu-added maraging stainless steel exhibits a superior combination of a yield strength of ~1.3 GPa, an elongation of ~15%, and an impact toughness of ~58 J.

Keywords: maraging stainless steel, TRIP effect, austenite reversion, Cu-rich nanoprecipitate

1. Introduction

Low carbon martensitic steels with high strength, ductility, and toughness are highly desirable for a variety of structural applications, such as aerospace and automotive industries [1,2]. However, increasing strength often leads to a decrease in ductility and toughness, which is known as the strength-ductility/toughness trade-off dilemma in structural materials [3-5]. Tremendous efforts have been put forth to break the strength-ductility/toughness trade-off of high-strength martensitic steels by introducing a certain amount of sub-micro/nanometer-sized retained or reverted austenite [6-9]. Reverted austenite often forms at the martensite lath boundaries, which is metastable and transforms to martensite during deformation, resulting in the transformation-induced plasticity (TRIP) effect. For example, Wang et al. [10] designed a TRIP-maraging steel containing 15 vol.% reverted austenite by controlling Mn contents, which exhibits a 1.1 GPa yield strength and 21% uniform elongation. Markfeld et al. [11] reported an 18% Ni (300) maraging steel containing 20 vol.% reverted austenite, which results in a marked

increase in tensile ductility. Sun et al. [12] reported that an intercritical tempering in the (austenite + martensite) dual-phase region promotes the austenite reversion of a Fe-5.42Mn-0.05C steel, leading to increased impact toughness through a TRIP assisted effect. Generally, martensite lath boundaries are preferred nucleation sites for the formation of reverted austenite, and the austenite stabilizers, such as Ni, Mn, Cu, and C, partition to the austenite region through controlled heat-treatments. The volume fraction of reverted austenite is highly dependent on the alloying additions and heat-treatment parameters. For achieving a substantial TRIP effect, 5-20 vol.% of reverted austenite is generally needed [10-13]. In addition, the appropriate size and composition of reverted austenite are also critical for tailoring the austenite stability. For example, Wang et al. [10] reported that reverted austenite with sizes in the range of 0.1-0.3 μm^2 is beneficial to the deformation-induced phase transformation. Yen et al. [14] reported that high contents of austenite stabilizing elements in the austenite could improve the stability of the austenite due to the increasing of chemical driving force for transformation. For this purpose, precipitation-hardened steels are often subjected to over-aging treatments at relatively high temperatures and/or for long times to facilitate elemental diffusion and partitioning [15,16]. However, the over-aging treatments inevitably cause the precipitate coarsening, leading to a severe attenuation of the precipitation hardening effect. In addition, a high level of Mn and C additions compromises the weldability of steels [17]. Therefore, achieving an accelerated austenite reversion without causing a significant reduction of precipitation hardening is highly desirable but still challenging.

Here, we report an innovative strategy to accelerate the austenite reversion by Cu-rich nanoprecipitates in maraging stainless steels. The precipitation behavior of Cu-rich

nanoprecipitates and their effects on the austenite reversion were systematically studied through high-resolution transmission electron microscopy (HR-TEM), atom probe tomography (APT), and electron back-scattered diffraction (EBSD). Particularly, the mechanisms for the Cu-assisted austenite revision and enhanced ductility and toughness were critically discussed. The findings provide a new approach to improve the strength-ductility-toughness synergy of high-strength martensitic steels.

2. Experimental

Fe-12.5Cr-7.5Ni-7.5Co-3.0Mo steels with and without 1 wt.% Cu were melted in a vacuum induction furnace and cast into ingots of 25 kg. Chemical compositions of the two steels are presented in Table 1. For simplicity, these two steels are hereafter referred to as the Cu-containing and Cu-free steels. The as-cast ingots were homogenized for 20 h at 1250 °C, hot-forged into square bars with a cross section of 40 × 40 mm and a length of 1300 mm, solutionized at 1050 °C for 1 h, immersed in liquid nitrogen for 1 h, and then aged at 500 °C for various periods of time. Cylindrical tensile samples with a diameter of 5 mm and a gauge length of 25 mm were prepared by electrodischarge machining. Room-temperature tensile tests were conducted on a MTS 810 testing machine at a strain rate of 2×10^{-3} s^{-1}. Charpy V-notch specimens were prepared to conduct the Charpy impact tests at room temperature.

The volume fraction of austenite was measured by X-ray diffractions (XRD) according to ASTM Standard E975-03 [18]. XRD samples with a dimension of 10 × 10 × 5 mm were wire-electrode cut and carefully polished, and they were tested in the solid form. Data collection was performed with a Bruker AXS D8 Advance X-ray diffractometer at a scanning rate of 1.0 °/min

using Cu K_α radiation in the 2θ range of 40-100°.

The precipitates were characterized by HR-TEM, and the distribution of austenite before and after tensile tests was measured by EBSD and TEM. APT needles were prepared by lift-out and tip milling in an FEI Scios focused ion beam/scanning electron microscope (FIB/SEM). APT experiments were performed in a CAMECA LEAP 5000 XR, and the Imago Visualization and Analysis Software (IVAS) 3.8 was used for three-dimensional reconstructions, composition analysis, and the creation of isoconcentration surfaces. Equilibrium phase fractions were calculated using the software Thermo-Calc 3.0.1 and TCFE7 database.

3. Results and discussion

The room-temperature engineering stress–strain curves of the two steels in the as-quenched and 60-h aged (peak aged) conditions are displayed in Fig. 1a. The Cu-containing and Cu-free steels exhibit similar tensile properties in the as-quenched state, with yield strengths of 713 ± 10 and 725 ± 11 MPa, respectively, and ultimate tensile strengths of 834 ± 14 and 883 ± 11 MPa, respectively. After aging for 60 h, the yield strengths of the Cu-containing and Cu-free steels increase to 1274 ± 18 and 1330 ± 15 MPa, respectively; both show a ~600 MPa increment in the yield strength. However, the aging treatment results in significantly different work-hardening behaviors and ductilities in the two steels. The work-hardening rate curves and true stress-strain curves of the two steels are illustrated in Fig. 1b, and their total and uniform elongations are summarized in Fig. 1c. In the Cu-free steel, after a precipitous initial drop associated with the elastic to plastic transition, the work-hardening rate decreases gradually possibly due to its ineffectiveness in dislocation generation and

accumulation during deformation. By contrast, in the Cu-containing steel, the work-hardening rate curve reveals a multi-stage work-hardening response; after the initial drop, the work-hardening rate increases substantially and maintains an obvious strain hardening plateau between the 3.5% and 7.5% true strains, followed by a gradual decrease. The Cu-free steel exhibit a slight work hardening with a uniform elongation of 5% and a total elongation of 11%, whereas, the Cu-containing steel shows a strong work hardening with a 9% uniform elongation and a 15% total elongation, demonstrating a substantial improvement in the ductility. The room-temperature Charpy impact energies of the two steels in the 60-h aged condition are also given in Fig. 1c. For the Cu-free steel, the impact resistance is low with an impact energy of 9 ± 1 J, which is typical for high-strength martensitic stainless steels [19]. In contrast, the impact energy of the Cu-containing steel is increased drastically to 58 ± 3 J, which is more than 6X higher than that of the Cu-free steel. The above results indicate that Cu plays an important role in improving the ductility and toughness of maraging stainless steels.

A representative TEM micrograph of the Cu-containing steel after aging for 60 h is shown in Fig. 2a. Two categories of nanoprecipitates were observed; one category (red arrows) with an average diameter of ~20 nm and located mainly on the dislocations, and the other category (orange arrows) with an average diameter of ~5 nm. High-resolution images of representative precipitates of the two categories and the corresponding fast Fourier transformation (FFT) patterns are presented in Fig. 2b-e. Figure 2b and c shows that the small precipitates are Cu particles with 9R twinned crystal structural, which is intermediate between the BCC and FCC structures and can be considered as a close-packed structure with stacking faults every third close-packed plane [20]. The orientation relationship between the 9R Cu particles and α-Fe

matrix is $(11\bar{4})_{9R} // (011)_{\alpha}$ and $[\bar{1}10]_{9R} // [1\bar{1}1]_{\alpha}$. Figure 2d and e shows that the crystal structure of the coarse precipitate is A_2B-type Laves phase. The chemical composition and solute partitioning of the two types of precipitates were further analyzed by APT, as shown in Fig. 2f-h. The iso-concentration surfaces of 10 at.% Cu (orange surface) and 10 at.% Mo (red surface) were used to visualize Cu-rich and Laves precipitates, respectively. Figure 2g and h shows the proximity histograms of Cu-rich and Mo-enriched precipitates, respectively. The Cu-rich precipitates consist of almost pure Cu in the precipitate core, whereas a clear segregation of Ni was observed at the Cu-precipitate/matrix heterophase interface; the Ni concentration reaches a maximum (18 at.%) at a distance of 1.0 nm from the interface. The composition of Mo-enriched precipitates is 38.2Fe-16.5Cr-8.4Ni-4.8Co-32.1Mo (at.%). The APT composition, together with the TEM results, indicates that Mo-enriched precipitates are $(Fe,Cr,Co,Ni)_2Mo$-type Laves phases.

The XRD patterns of the Cu-free and Cu-containing steels in the as-quenched and different aged conditions are displayed in Fig. 3a and b, respectively. In the as-quenched condition, both steels exhibit diffraction peaks corresponding to BCC-Fe only, with no signs of FCC-Fe, indicating that the as-quenched steels has an almost fully martensitic microstructure. Upon aging at 500 °C, the two steels exhibit different XRD characteristics. In the Cu-free steel, no austenite peaks can be observed in the 0.5-h aged condition, and the austenite peaks appear but with a low intensity in the 24-h and 60-h aged condition. Quantitative analyses (Fig. 3c) indicate that the volume fractions of the austenite phase in the 0.5-h, 24-h, and 60-h aged conditions are 0, 5.0 ± 0.8%, and 6.5 ± 0.6%, respectively, implying that the martensite-to-austenite reversion kinetics is slow in the Cu-free steel. By contrast, obvious peaks of reverted

austenite were detected in the Cu-containing steel in all the aged conditions; the volume fractions of the austenite phase in the 0.5-h, 24-h, and 60-h aged conditions are 8.5 ± 0.8%, 10.8 ± 0.7%, and 12.4 ± 1.2%, respectively. EBSD phase map of the Cu-containing steel in the 60-h aged condition is displayed in Fig. 3d. According to the phase map, the volume fraction of reverted austenite (blue area) was estimated to be 11.8%, which is in good agreement with the XRD data. The high volume fraction of reverted austenite in the Cu-containing steel suggests that the Cu addition accelerates the austenite reversion kinetics.

The detailed microstructure of reverted austenite in the Cu-containing steel after aging for 60 h was further analyzed by TEM and APT, and the results are shown in Fig. 4. From Fig. 4a, film-like austenite was observed mostly at lath boundaries, whereas some granular austenite appears in the martensitic matrix. The orientation relationship between the reverted austenite and martensite matrix obeys the Nishiyama–Wasserman relationship, i.e., $[01\bar{1}]_\gamma$ // $[001]_\alpha$ and $(111)_\gamma$ // $(110)_\alpha$ (Fig. 4b) [21,22]. Figure 4c and d is the bright-field TEM image and the corresponding TEM/EDS elemental mapping of Ni, Cu, and Mo, respectively. The reverted austenite is enriched in Ni, and its substructure consists of stacking faults and a low density of dislocations, suggesting that the formation of reverted austenite occurs by a process of nucleation and growth. More intriguingly, a considerable amount of reverted austenite is co-precipitated with Cu-rich precipitates, with the former adjacent to or enveloping the latter.

To understand the formation mechanism of reverted austenite, it is essential to characterize the solute partitioning and phase composition at the nanoscale. Figure 4e shows the APT microstructure of the austenite and Cu-rich precipitates in the Cu-containing steel after aging for 60 h. The iso-concentration surfaces of 20 at.% Ni (green surface) and 10 at.% Cu (orange

surface) were used to visualize reverted austenite and Cu-rich precipitates, respectively. Three Cu-rich precipitates were detected in the volume of analysis; two are adjacent to the austenite phase and one is encompassed within the austenite phase. The co-precipitation structure of reverted austenite and Cu-rich precipitates is consistent with the TEM results (cf. Fig. 4c and d). The proximity histogram of reverted austenite (Fig. 4f) reveals that the Ni concentration is approximately 30 at.%, which is 6X higher than that in the martensitic matrix (5 at.%), indicating that the growth of reverted austenite is accompanied by Ni diffusion. In addition, Cu is also enriched in the reverted austenite (0.8 at.%), as compared with that in the matrix (0.4 at.%). These observations indicate that the diffusion of both Ni and Cu are involved in the austenite reversion of the Cu-containing steel.

The XRD spectra and EBSD phase maps of the tensile-deformed Cu-containing steel are presented in Fig. 5a and b, respectively. After tensile deformation, the Cu-containing steel has a fully martensitic microstructure with no detectable reverted austenite. The deformation microstructures were further characterized by TEM, as shown in Fig. 5c. Almost all reverted austenite transforms into martensite after the tensile deformation, and numerous dislocations are accumulated in and around the deformation-induced martensite. The deformation-induced austenite to martensite transformation can enhance the work-hardening rate via two mechanisms [23]: (i) composite strengthening due to the formation of hard martensite phase and (ii) formation of dislocations in and around newly formed martensite regions as a result of the volume expansion during the austenite to martensite transformation. Therefore, it is reasonable to speculate that the enhanced work-hardening rate of the Cu-containing steel is due to the deformation-induced austenite to martensite transformation. The enhancement of the

work hardening makes the conditions for plastic instability to be met at higher strains, so that the onset of necking is postponed to large deformations. As a result, an increase in the uniform elongation and ultimate tensile stress was observed in the Cu-containing steel.

As aforementioned, the formation of reverted austenite is a diffusion-controlled process, which is related to the nucleation and growth of reverted austenite [24]. The effect of Cu on the austenite reversion can be analyzed from the nucleation point of view. First, because Cu is an austenite stabilizing element, the addition of Cu to maraging stainless steels increases the total concentration of austenite forming elements, resulting in an increase in the chemical driving force for the formation of reverted austenite. To quantitatively understand how the Cu addition affects the thermodynamic equilibrium, the equilibrium volume fractions of austenite phase in the Cu-free and Cu-containing steels were calculated by using Thermo-Calc, and the calculation results are shown in supplementary Fig. S1. At 500 ºC, the volume fraction of austenite in the Cu-free and Cu-containing steels are 10.6% and 12.0%, respectively. Therefore, the Cu addition substantially increases the equilibrium volume fraction of austenite and enhances the chemical driving force for the austenite reversion. Second, the Cu-rich nanoprecipitates promote the nucleation of reverted austenite through interfacial segregation. Cu has a very low solubility (~0.2 at.%) in BCC-Fe at 500 ºC and quickly precipitates as coherent bcc clusters in the martensitic matrix during aging [25]. The heat of mixing between Fe–Cu is positive and large (+13 kJ mol^{-1}), whereas that for both Fe–Ni and Cu–Ni pairs are very small (–4 and +2 kJ mol^{-1}, respectively); this means that the segregation of Ni at the interface between Cu-rich precipitates and matrix can act a buffer layer to reduce the interfacial energy of Cu precipitates [26]. Therefore, it is energetically favorable for Ni to segregate at the

interfaces between Cu-rich precipitates and matrix. Ni is known as one of the major austenite forming elements in the steels, the Ni-enriched regions at the Cu-precipitate/matrix interface provide the chemical conditions for the phase transformation from martensite to austenite. Furthermore, the interfaces between Cu-rich precipitates and matrix can act as preferential nucleation sites for heterogeneous nucleation of reverted austenite. As a result, the increased chemical driving force and population of nucleation sites (heterophase interfaces), together with the Ni enrichment at the interfaces, substantially increase the nucleation rate of reverted austenite. Consequently, the volume fraction of reverted austenite in the Cu-containing steel (~12.4 vol.%) is much higher than that in the Cu-free steel without Cu additions (~6.5 vol.%). Furthermore, the TRIP behavior in the plastic zone around a front fracture absorbs fracture energy, effectively contributing to the improvement of toughness [27]. Consequently, a substantial improvement in ductility and toughness was observed in the Cu-containing steel with the TRIP effect (cf. Fig. 1). Therefore, our work provides a new strategy to accelerate the austenite reversion and enhance the TRIP effect of maraging steels through Cu nanoprecipitation. The Cu content used here is 1 wt.%, which is lower than that in commercial Cu-containing steels, such as 17-4 PH and 15-5 PH stainless steels [28,29]; thus, this Cu content should be readily achievable in industrial scale steels.

4. Conclusions

The effects of Cu precipitation on the austenite reversion and mechanical properties of maraging stainless steels were systematically investigated. Our results indicate that Cu, as an austenite stabilizer, increases the equilibrium austenite fraction and enhances the chemical

driving force for the austenite formation. In addition, Cu-rich precipitates significantly promote the nucleation of reverted austenite by not only increasing the chemical driving force for nucleation, but also providing high number densities of heterogeneous nucleation sites for the austenite reversion. During tensile deformation, the metastable reverted austenite transforms to martensite, which substantially improves the ductility and toughness through the TRIP effect. The Cu-containing steel containing 12.4 vol.% reverted austenite has a yield strength of 1330 MPa, an elongation of 15%, and an impact toughness of 58 J, exhibiting a good combination of strength, ductility, and toughness. The strategy of Cu-assisted austenite reversion should be applicable to many other steels and provides a new approach to improve the strength-ductility-toughness synergy of advanced high-strength steels.

Acknowledgements

Z.B.J. acknowledges the financial support from the National Natural Science Foundation of China (51801169), State Key Laboratory for Advanced Metals and Materials Open Fund (2017-ZD01), Chinese National Engineering Research Centre for Steel Construction (Hong Kong Branch) at PolyU (P0013862), and Guangzhou International Science & Technology Cooperation Program (201907010026). W.W. acknowledges the financial support from the Youth Innovation Promotion Association of Chinese Academy of Sciences (2017233), the Innovation Project of Institute of Metal Research (2015-ZD04), the National Natural Science Foundation of China Research Fund for International Young Scientists (No. 51750110515), and the National Natural Science Foundation of China (No. 51472249).

References

[1] B.B. He, B. Hu, H.W. Yen, G.J. Cheng, Z.K. Wang, H.W. Luo, M.X. Huang, High Dislocation Density-Induced Large Ductility in Deformed and Partitioned Steels, Science 357(6355) (2017) 1029-1032.

[2] W. Xu, P.E.J. Rivera-Díaz-del-Castillo, W. Yan, K. Yang, D. San Martín, L.A.I. Kestens, S. van der Zwaag, A New Ultrahigh-strength Stainless Steel Strengthened by Various Coexisting Nanoprecipitates, Acta Mater. 58(11) (2010) 4067-4075.

[3] S. Jiang, H. Wang, Y. Wu, X.J. Liu, H.H. Chen, M.J. Yao, B. Gault, D. Ponge, D. Raabe, A. Hirata, M.W. Chen, Y.D. Wang, Z.P. Lu, Ultrastrong Steel via Minimal Lattice Misfit and High-Density Nanoprecipitation, Nature 544(7651) (2017) 460-464.

[4] H. Luo, X. Wang, Z. Liu, Z. Yang, Influence of Refined Hierarchical Martensitic Microstructures on Yield Strength and Impact Toughness of Ultra-high Strength Stainless Steel, J. Mater. Sci. Technol. 51 (2020) 130-136.

[5] J. Yan, H. Xu, X. Zuo, T. Jia, E. Wang, Strategies for Strengthening-Ductility and Hierarchical Co-precipitation in Multicomponent Nano-precipitated Steels by Cu Partitioning, Mater. Sci. Eng., A 739 (2019) 225-234.

[6] Q. Liu, J. Gu, C. Li, Regulation of Cu Precipitation by Intercritical Tempering in a HSLA Steel, J. Mater. Res. 29(8) (2014) 950-958.

[7] Y. Ma, W. Song, S. Zhou, A. Schwedt, W. Bleck, Influence of Intercritical Annealing Temperature on Microstructure and Mechanical Properties of a Cold-Rolled Medium-Mn Steel, Metals 8(5) (2018) 357.

[8] W.W. Sun, Y.X. Wu, S.C. Yang, C.R. Hutchinson, Advanced High Strength Steel (AHSS) Development through Chemical Patterning of Austenite, Scripta Mater. 146 (2018) 60-63.

[9] X.L. Wu, M.X. Yang, F.P. Yuan, L. Chen, Y.T. Zhu, Combining Gradient Structure and TRIP Effect to Produce Austenite Stainless Steel with High Strength and Ductility, Acta Mater. 112 (2016) 337-346.

[10] M.M. Wang, C.C. Tasan, D. Ponge, D. Raabe, Spectral TRIP Enables Ductile 1.1 Gpa Martensite, Acta Mater. 111 (2016) 262-272.

[11] A. Markfeld, A. Rosen, The Effect of Reverted Austenite on the Plastic Deformation of Maraging Steel, Mater. Sci. Eng. 46(2) (1980) 151-157.

[12] C. Sun, S.L. Liu, R.D.K. Misra, Q. Li, D.H. Li, Influence of Intercritical Tempering Temperature on Impact Toughness of a Quenched and Tempered Medium-Mn Steel: Intercritical Tempering Versus Traditional Tempering, Mater. Sci. Eng., A 711 (2018) 484-491.

[13] E.I. Galindo-Nava, W.M. Rainforth, P.E.J. Rivera-Díaz-del-Castillo, Predicting Microstructure and Strength of Maraging Steels: Elemental Optimisation, Acta Mater. 117 (2016) 270-285.

[14] H.-W. Yen, S.W. Ooi, M. Eizadjou, A. Breen, C.-Y. Huang, H.K.D.H. Bhadeshia, S.P. Ringer, Role of Stress-assisted Martensite in the Design of Strong Ultrafine-grained Duplex Steels, Acta Mater. 82 (2015) 100-114.

[15] U.K. Viswanathan, G.K. Dey, V. Sethumadhavan, Effects of Austenite Reversion During Overageing on the Mechanical Properties of 18 Ni (350) Maraging Steel, Mater. Sci. Eng. A 398(1-2) (2005) 367-372.

[16] A.J. Knowles, P. Gong, K.M. Rahman, W.M. Rainforth, D. Dye, E.I. Galindo-Nava, Development of Ni-free Mn-stabilised Maraging Steels Using Fe_2SiTi Precipitates, Acta Mater. 174 (2019) 260-270.

[17] H.J. Kong, T. Yang, R. Chen, S.Q. Yue, T.L. Zhang, B.X. Cao, C. Wang, W.H. Liu, J.H. Luan, Z.B. Jiao, B.W. Zhou, L.G. Meng, A. Wang, C.T. Liu, Breaking the Strength-Ductility Paradox in Advanced Nanostructured Fe-Based Alloys through Combined Cu and Mn Additions, Scripta Mater. 186 (2020) 213-218.

[18] ASTM International, E975-03, Standard Practice for X-Ray Determination of Retained Austenite in Steel with Near Random Crystallographic Orientation (ASTM International, 2008).

[19] Z. Guo, W. Sha, E.A. Wilson, R.W. Grey, Improving Toughness of PH13-8 Stainless Steel through Intercritical Annealing, ISIJ Int. 43(10) (2003) 1622-1629.

[20] M.L.J. P.J. Othen, G.D.W. Smith, W. J. Phythian, Transmission Electron Microscope Investigations of the Structure of Copper Precipitates in Thermally-aged Fe–Cu and Fe–Cu–Ni, Philos. Mag. Lett. 64 (1991) 383-391.

[21] Z. Nishiyama, X-ray Investigation of the Mechanism of the Transformation from Face-centered Cubic Lattice to Body-centered Cubic, Sci. Rep. Res. Inst. Tohoku Univ. 23 (1934) 638.

[22] G. Wassermann, Influence of the α-γ Transformation of an Irreversible Nickel on Crystal Orientation and Tensile Strength, Arch. Eisenhüttenwes 16 (1933) 647.

[23] P. Jacques, Q. Furnémont, A. Mertens, F. Delannay, On the Sources of Work Hardening in Multiphase Steels Assisted by Transformation-induced Plasticity. Philos. Mag. A 81(7) (2001) 1789-1812.

[24] A.P. Miodownik, N. Saunders, Modelling of Materials Properties in Duplex Stainless Steels, Mater. Sci. Technol. 18(8) (2013) 861-868.

[25] Y.U. Heo, Y.K. Kim, J.S. Kim, J.K. Kim, Phase Transformation of Cu Precipitates from Bcc to Fcc in Fe–3Si–2Cu Alloy, Acta Mater. 61(2) (2013) 519-528.

[26] Z.B. Jiao, J.H. Luan, Z.W. Zhang, M.K. Miller, W.B. Ma, C.T. Liu, Synergistic Effects of Cu and Ni on Nanoscale Precipitation and Mechanical Properties of High-Strength Steels, Acta Mater. 61(16) (2013) 5996-6005.

[27] S.S. Xu, Y. Zhao, D. Chen, L.W. Sun, L. Chen, X. Tong, C.T. Liu, Z.W. Zhang, Nanoscale Precipitation and Its Influence on Strengthening Mechanisms in an Ultra-High Strength Low-Carbon Steel, Int. J. Plasticity. 113 (2018) 99-110.

[28] Z.M. Wang, H. Li, Q. Shen, W.Q. Liu, Z.Y. Wang, Nano-precipitates Evolution and Their Effects on Mechanical Properties of 17-4 Precipitation-hardening Stainless Steel, Acta Mater. 156 (2018) 158-171.

[29] L. Couturier, F. De Geuser, M. Descoins, A. Deschamps, Evolution of the Microstructure of a 15-5PH Martensitic Stainless Steel during Precipitation Hardening Heat Treatment, Mater. Design 107 (2016) 416-425.

Figure captions

Fig. 1 Mechanical properties of the Cu-free and Cu-containing steels: (a) engineering tensile stress-strain curves of the steels in the as-quenched and 60-h aged conditions, (b) work hardening rate curves and true stress-strain curves of the steels in the 60-h aged condition, and (c) elongations and Charpy impact energies in the 60-h aged condition.

Fig. 2 Microstructure of Mo-enriched and Cu-rich precipitates: (a) bright-field TEM image of the Cu-containing steel in the 60-h aged condition, HR-TEM images of (b) 9R Cu and (d) Laves phase, (c) and (e) are the corresponding FFT patterns of (b) and (d), respectively, (f) APT microstructure of Cu-rich and Mo-enriched precipitates, and (g) and (h) are the proximity histograms of Cu-rich and Mo-enriched precipitates, respectively.

Fig. 3 Microstructure of reverted austenite before deformation: XRD patterns of the (a) Cu-free and (b) Cu-containing steels in the as-quenched and aged conditions, (c) volume fractions of reverted austenite as a function of aging time, (d) EBSD phase maps for the Cu-containing steel in the 60-h aged condition.

Fig. 4 Microstructure of reverted austenite before deformation: (a) the TEM micrographs of the Cu-containing steel in the 60-h condition, (b) the SAED patterns corresponding to reverted austenite and matrix in (a), (c) and (d) are the bright-field TEM image and corresponding TEM/EDS elemental mapping of Ni, Cu and Mo, respectively, and (e) and (f) APT microstructure and compositions of Cu-rich precipitates and reverted austenite.

Fig. 5 Microstructure of reverted austenite after deformation: (a) XRD pattern, (b) EBSD phase maps, and (c) bright-field TEM image of the Cu-containing steel after tensile deformation.

Figure 1

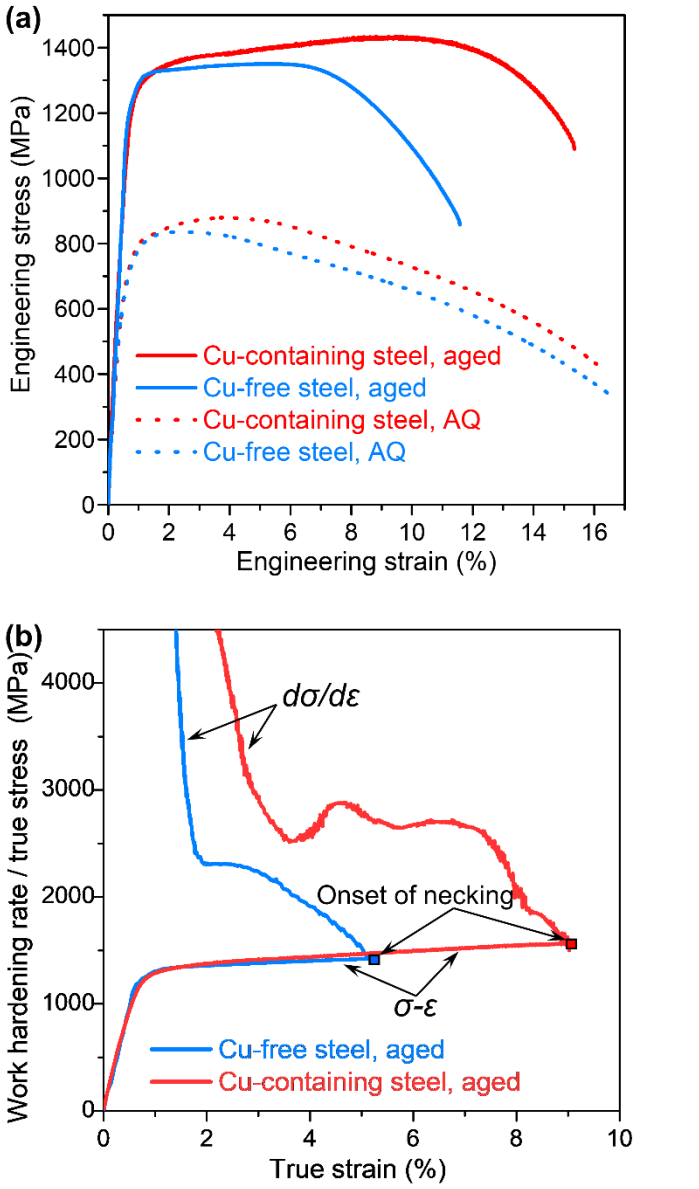

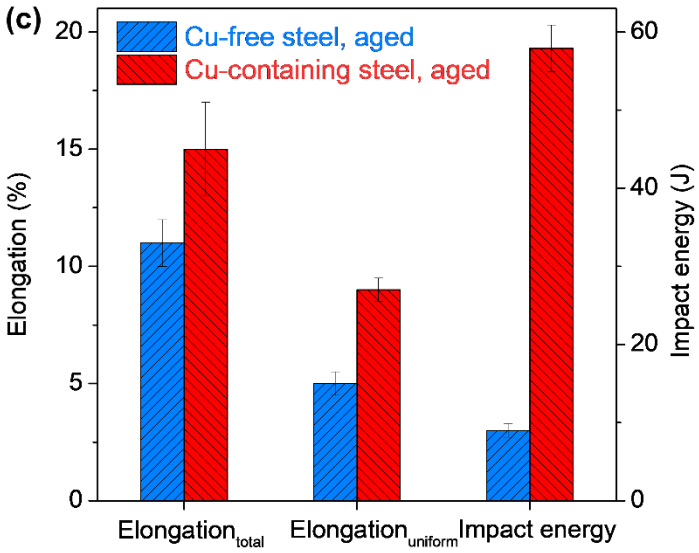

Figure 2

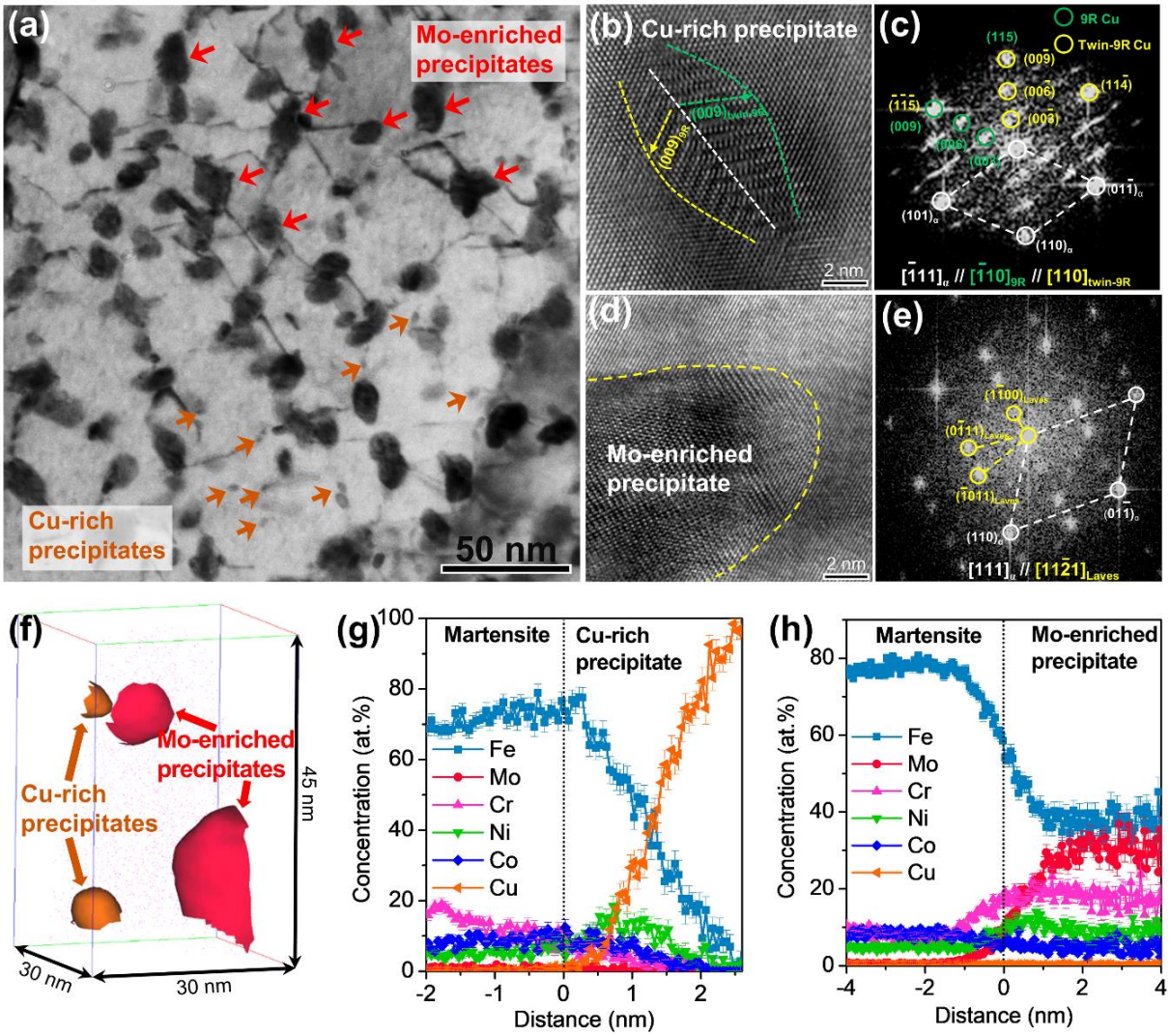
(a)
Mo-enriched precipitates
Cu-rich precipitates
50 nm
(b) Cu-rich precipitate
2 nm
(c)
9R Cu
Twin-9R Cu
[111]α // [110]9R // [110]twin-9R
(d)
Mo-enriched precipitate
2 nm
(e)
[111]α // [112]Laves
(f)
Mo-enriched precipitates
Cu-rich precipitates
45 nm
30 nm
30 nm
(g)
Martensite
Cu-rich precipitate
Concentration (at.%)
Fe
Mo
Cr
Ni
Co
Cu
Distance (nm)
(h)
Martensite
Mo-enriched precipitate
Concentration (at.%)
Fe
Mo
Cr
Ni
Co
Cu
Distance (nm)

Figure 3

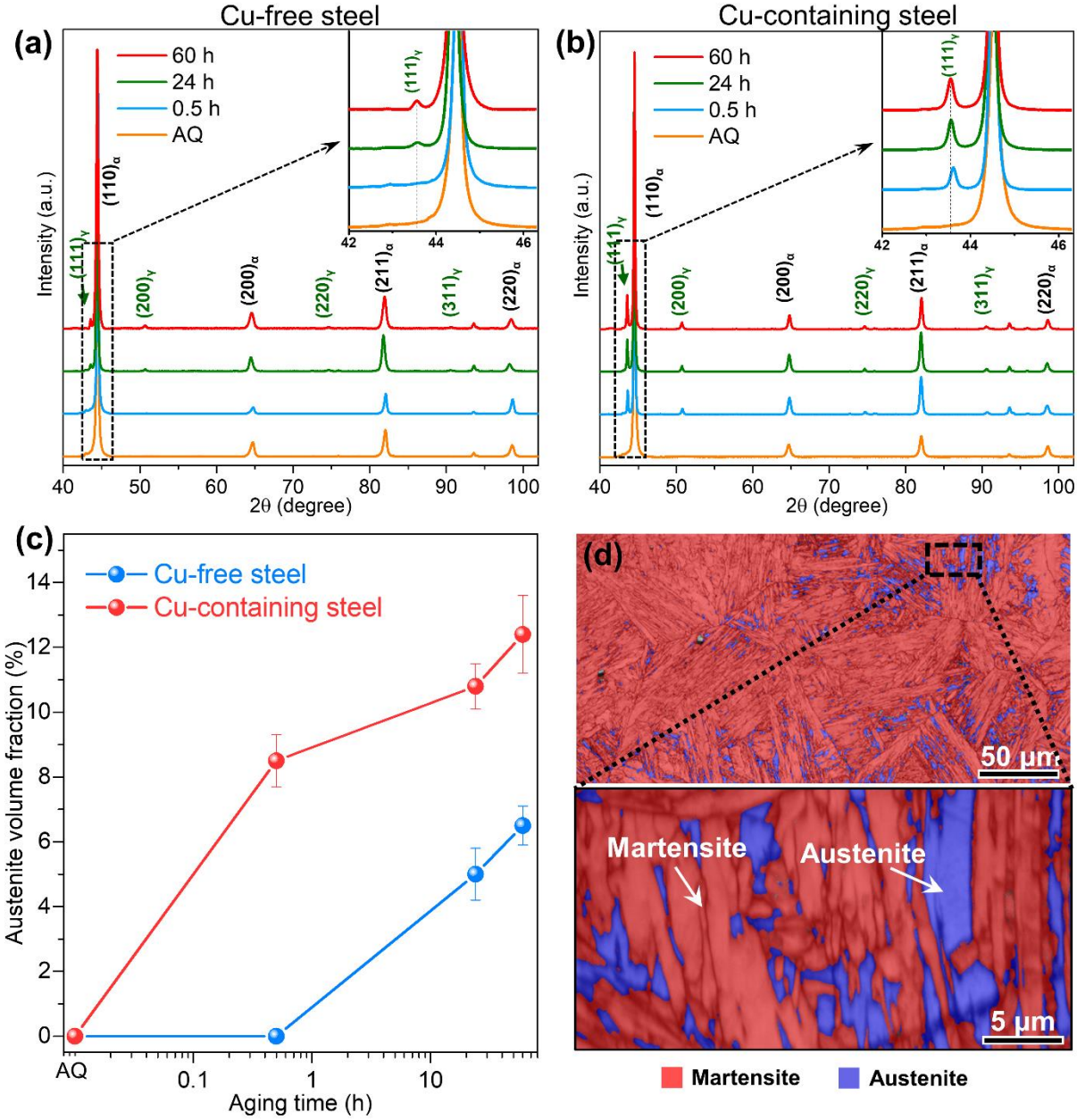
Cu-free steel
Cu-containing steel
(a)
(b)
60 h
24 h
0.5 h
AQ
Intensity (a.u.)
2θ (degree)
(c)
Cu-free steel
Cu-containing steel
Austenite volume fraction (%)
Aging time (h)
AQ
(d)
50 μm
Martensite
Austenite
5 μm
Martensite
Austenite

Figure 4

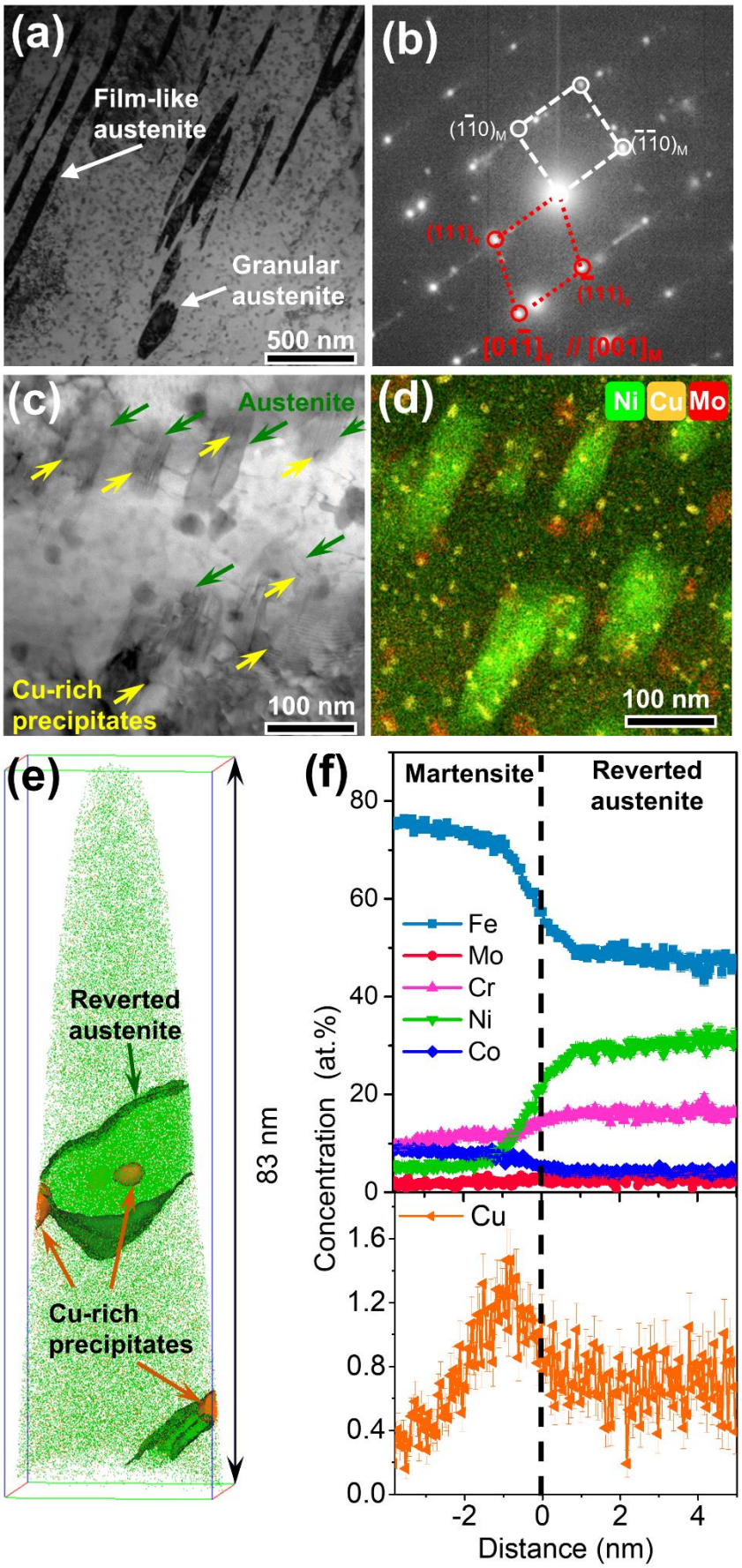
(a)
Film-like austenite
Granular austenite
500 nm
(b)
(1̄10)M
(1̄1̄0)M
(111)γ
(111)γ
[01̄1̄]γ // [001]M
(c)
Austenite
Cu-rich precipitates
100 nm
(d)
Ni Cu Mo
100 nm
(e)
Reverted austenite
Cu-rich precipitates
83 nm
(f)
Martensite
Reverted austenite
Fe
Mo
Cr
Ni
Co
Cu
Concentration (at.%)
Distance (nm)

Figure 5

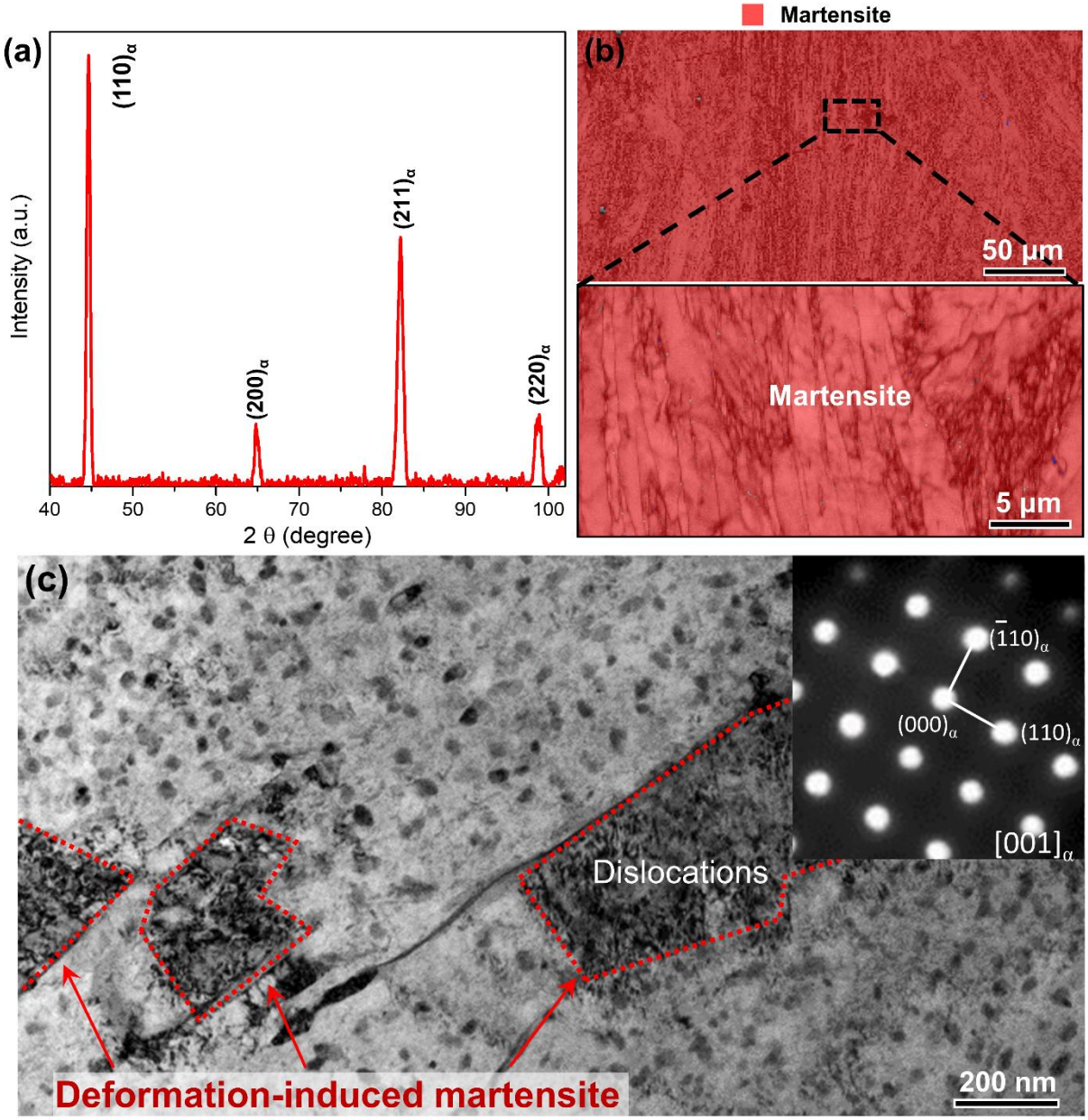
(a)
(110)α
(200)α
(211)α
(220)α
Intensity (a.u.)
40
50
60
70
80
90
100
2 θ (degree)
Martensite
(b)
50 μm
Martensite
5 μm
(c)
(110)α
(000)α
(110)α
[001]α
Dislocations
Deformation-induced martensite
200 nm